Production Engineering (2020) 14:123–134
https://doi.org/10.1007/s11740-019-00937-9

PRODUCTION PROCESS

On mesh dependencies in finite-element-based damage prediction: application to sheet metal bending

Leon Sprave[1] · Alexander Schowtjak[2] · Rickmer Meya[2] · Till Clausmeyer[2] · A. Erman Tekkaya[2] · Andreas Menzel[1,3]

Received: 8 August 2019 / Accepted: 11 November 2019 / Published online: 25 November 2019

Abstract
The properties of a local and a regularised gradient-enhanced continuum damage model are highlighted and both types of models are applied to the simulation of an air bending process. Constitutive relations are summarised for both Lemaitre-type models and a brief description of their implementation into Abaqus user material subroutines is given. With (several) material parameters obtained from a basic parameter identification process, an air bending experiment is simulated with different mesh densities. By means of the damage evolution as well as the distribution of representative damage and hardening variables, the mesh dependence of the local model in contrast to the mesh independence of the gradient-enhanced model is analysed for two air bending processes with different die width.

Keywords Ductile damage · Finite element method · Regularisation · Air bending

1 Introduction

Continuum damage mechanics are related to the modelling of degradation phenomena in solid continua. The simulation of such damage effects in the context of the finite element method typically is accompanied by mesh dependent results, unless additional regularisation techniques are included. Originally, non-local theories using an integral value of a locally defined damage variable have been proposed in order to obtain a regularised and mesh independent response, see e.g. [2, 3] and are still used today [15]. Thereafter, gradient models were established as an alternative regularisation method, see e.g. [27] for an approach using the second-order gradient of deformation, [6] addressing different regularisation approaches in the context of finite elements or [20] for a discussion of strain-gradients to regularise a continuum damage model. Gradient approaches have since been further developed, see e.g. [7] or see [9] for the introduction of the micromorphic approach. In [30] a gradient-enhanced continuum damage model coupled to plasticity is described and in [21] gradient-enhanced continuum damage is applied to a contact problem.

A typical example for damage effects significantly influencing material properties in metal forming is bending in sheet metal forming. Suitable material models must predict a ductile damage response, i.e. damage phenomena stemming from e.g. coalescence of micro-voids developing in combination with large plastic deformations. In the framework of continuum damage mechanics, two main approaches to model ductile damage have been established: The micromechanically motivated damage model includes the concept of a void volume fraction—as proposed by Gurson [10] and further developed by Tvergaard and Needleman [28] and Rousselier [22]—and is based on the assumption that damage evolution influences plasticity related quantities only rather than elastic material properties. Lemaitre-type damage evolution, as established in [14, 17], however, also affects the elastic properties of the material. Both approaches have extensively been studied and further developed, see e.g. the review [4] which particularly deals with damage in bulk metal forming.

Fracture under bending-type loading usually starts within the so-called outer fibres—the area that undergoes the highest level of tensile strains within the bending process. The macroscopic development of ductile fracture is discussed

✉ Leon Sprave
leon.sprave@tu-dortmund.de

[1] Institute of Mechanics, TU Dortmund, Leonhard-Euler-Str., 44227 Dortmund, Germany

[2] Institut für Umformtechnik und Leichtbau, TU Dortmund, Baroper Str. 303, 44227 Dortmund, Germany

[3] Division of Solid Mechanics, Lund University, P.O. Box 118, 221 00 Lund, Sweden

in [1] with special focus on aluminium. Initiation of ductile fracture starts with a roughening of the surface denoted as orange peel. With increasing deformation rough notches at the outer fibres parallel to the bending line develop. Eventually, shearing occurs and finally a macroscopic crack evolves. Damage evolution could be shown as one possible reason for the evolution of such notches, see [23]. Moreover, fracture initiation at the notches is characterised by a ductile fracture mode in combination with a localised deformation, see [24]. For a DP780-steel, it has been shown that void nucleation and coalescence take place prior to localisation, see [12]. Moreover, the influence of the stress state on the damage evolution was discussed in the context of bending experiments in [18], whereby a stress superposition approach was applied. In addition, an increasing void area fraction towards the outer fibre was revealed. Furthermore, nearly no voids have been observed at the inner fibre during plastic bending of DP800 steels, see [18]. Initiation of fracture could accurately be predicted in [8].

In this work a local Lemaitre-type model based on [16, 25] is compared with a gradient-enhanced Lemaitre-type model based on [26], which extends the small strain model [13] to a finite deformation setting. Emphasis is put upon the comparison of mesh dependence—or rather mesh independence—and not upon the comparison of differences in the modelling details. To this end, the continuum damage framework is briefly summarised in Sect. 2 and the local and gradient-enhanced models are specified in Sects. 2.1 and 2.2 respectively. Section 3 describes the basic parameter identification process, before results of air bending simulations with different mesh densities and die widths are presented in Sect. 4 for both models. Finally, Sect. 5 summarises the paper and provides a short outlook for possible future research.

2 Continuum damage modelling

Consider a body with reference configuration $\mathcal{B}_0$ and referential position vectors $\boldsymbol{X} \in \mathcal{B}_0$. The current, respectively spatial configuration at time t shall be denoted as $\mathcal{B}_t$ with spatial position vectors $\boldsymbol{x}$ related to referential placements by the non-linear deformation mapping $\boldsymbol{x} = \boldsymbol{\varphi}(\boldsymbol{X}, t)$. The deformation gradient is introduced as $\boldsymbol{F} = \nabla_{\boldsymbol{X}} \boldsymbol{\varphi}$ with its determinant $J = \det(\boldsymbol{F}) > 0$. The deformation gradient is assumed to be multiplicatively decomposed into an elastic and a plastic part, i.e. $\boldsymbol{F} = \boldsymbol{F}^{\mathrm{e}} \cdot \boldsymbol{F}^{\mathrm{p}}$. Based on this, the elastic Finger tensor $\boldsymbol{b}^{\mathrm{e}} = \boldsymbol{F}^{\mathrm{e}} \cdot \boldsymbol{F}^{\mathrm{e\,t}}$, placed in the spatial configuration, and the elastic right Cauchy-Green tensor $\boldsymbol{C}^{\mathrm{e}} = \boldsymbol{F}^{\mathrm{e\,t}} \cdot \boldsymbol{F}^{\mathrm{e}}$, settled in the so-called intermediate configuration, can be introduced and give rise to related logarithmic strain tensors, to be specific

$$\boldsymbol{E}_0^{\mathrm{e}} = \tfrac{1}{2} \ln(\boldsymbol{C}^{\mathrm{e}}) \,, \qquad \boldsymbol{\varepsilon}^{\mathrm{e}} = \tfrac{1}{2} \ln(\boldsymbol{b}^{\mathrm{e}}) \,. \tag{1}$$

In order to model proportional hardening, a scalar-valued hardening variable $\alpha \geq 0$ is introduced. Moreover, isotropic damage shall be modelled via the scalar-valued damage variable d with $0 \leq d < 1$, where $d = 0$ corresponds to the undamaged state.

With these variables at hand, the Helmholtz energy shall be assumed to adhere to the format

$$\Psi(\boldsymbol{E}_0^{\mathrm{e}} \text{ or } \boldsymbol{\varepsilon}^{\mathrm{e}}, d, \alpha) = \Psi^{\mathrm{e}}(\boldsymbol{E}_0^{\mathrm{e}} \text{ or } \boldsymbol{\varepsilon}^{\mathrm{e}}, d) + \Psi^{\mathrm{p}}(\alpha) \,. \tag{2}$$

Adopting the framework of standard dissipative material, one identifies the related thermodynamic driving forces as

$$\begin{aligned} \boldsymbol{m}^{\mathrm{t}} &:= 2 \frac{\partial \Psi}{\partial \boldsymbol{b}^{\mathrm{e}}} \cdot \boldsymbol{b}^{\mathrm{e}} \quad \text{or} \quad \boldsymbol{M}^{\mathrm{t}} := 2 \boldsymbol{C}^{\mathrm{e}} \cdot \frac{\partial \Psi}{\partial \boldsymbol{C}^{\mathrm{e}}} \,, \\ q &:= - \frac{\partial \Psi}{\partial d} \,, \qquad \beta := - \frac{\partial \Psi}{\partial \alpha} \,, \end{aligned} \tag{3}$$

namely the Mandel stresses $\boldsymbol{m}$ (here represented for the elastically isotropic case) or $\boldsymbol{M}$, settled in the spatial respectively intermediate configuration, the damage driving force q and the hardening stress β.

Inelastic processes resulting in the evolution of plasticity and damage are modelled by means of a dissipation potential $\Phi(\boldsymbol{m} \text{ or } \boldsymbol{M}, \beta, q, d)$, which can be split into a plasticity related and a damage related contribution and which is dependent on the driving forces and the damage d. The evolution of the plastic part of the deformation gradient can be represented by the plastic velocity gradient $\boldsymbol{L}^{\mathrm{p}} = \dot{\boldsymbol{F}}^{\mathrm{p}} \cdot \boldsymbol{F}^{\mathrm{p\text{-}1}}$, whereby the notation $\dot{\bullet}$ denotes the material time derivative. Similar to $\boldsymbol{C}^{\mathrm{e}}$, $\boldsymbol{L}^{\mathrm{p}}$ is settled in the intermediate configuration. A push forward operation results in $\boldsymbol{l}^{\mathrm{p}} = \boldsymbol{F}^{\mathrm{e}} \cdot \boldsymbol{L}^{\mathrm{p}} \cdot \boldsymbol{F}^{\mathrm{e}-1}$ which, by analogy with $\boldsymbol{b}^{\mathrm{e}}$, is placed in the spatial configuration. Based on this, associated evolution equations result in

$$\begin{aligned} \boldsymbol{l}^{\mathrm{p}} &= \lambda \frac{\partial \Phi}{\partial \boldsymbol{m}^{\mathrm{t}}} \quad \text{or} \quad \boldsymbol{L}^{\mathrm{p}} = \lambda \frac{\partial \Phi}{\partial \boldsymbol{M}^{\mathrm{t}}} \,, \\ \dot{d} &= \lambda \frac{\partial \Phi}{\partial q} \,, \qquad \dot{\alpha} = \lambda \frac{\partial \Phi}{\partial \beta} \,, \end{aligned} \tag{4}$$

with a single Lagrange multiplier λ related to the corresponding Karush–Kuhn–Tucker (KKT) conditions

$$\Phi \leq 0, \quad \lambda \geq 0, \quad \lambda \Phi = 0. \tag{5}$$

It is remarked that separate activation of plasticity and damage evolution requires the introduction of two sets of KKT conditions and two Lagrange multipliers.

In the following subsections, the energy and dissipation potentials shall be specified for a local and a gradient-enhanced Lemaitre-type model.

2.1 Local Lemaitre model

The local Lemaitre model shall be formulated in terms of arguments settled in the intermediate configuration. To be specific, the elastic energy contribution to the Helmholtz energy is assumed as

$$\Psi^{\mathrm{e}}(\boldsymbol{E}_0^{\mathrm{e}}, d) = [\,1-d\,]\,\big[\,\tfrac{1}{2}\,\lambda_0 \mathrm{tr}^2(\boldsymbol{E}_0^{\mathrm{e}}) + \mu_0 \mathrm{tr}\big(\boldsymbol{E}_0^{\mathrm{e}\,2}\big)\,\big]\,, \tag{6}$$

with Lamé parameters λ_0 and μ_0. The proportional hardening form adopted is of Swift-type, namely

$$\Psi^{\mathrm{p}}(\alpha) = \frac{A}{n+1}\,\big[\alpha_0+\alpha\big]^{n+1}\,, \tag{7}$$

with material parameters A, n and α_0. For the dissipation potential an additive split into plastic and damage parts is assumed, i.e. $\Phi = \Phi^{\mathrm{p}} + \Phi^{\mathrm{d}}$, whereby the plastic part chosen is a von Mises yield criterion including effective equivalent stresses, i.e.

$$\Phi^{\mathrm{p}}(\boldsymbol{M}, \beta; d) = \frac{\|\mathrm{dev}(\boldsymbol{M}^{\mathrm{t}})\|}{1-d} - \beta\,. \tag{8}$$

It is remarked that the yield function $\Phi^{\mathrm{p}} \leq 0$ is used for the KKT conditions to determine the (single) Lagrange multiplier. For the damage part of the dissipation potential a modified damage driving force

$$\widehat{q} := \frac{1}{\mu_0}\,\sum_{i=1}^{3}\,\left\langle \frac{M_i}{1-d}\right\rangle^2 - \frac{\lambda_0}{3\,\lambda_0\,\mu_0 + 2\,\mu_0^2}\left\langle \frac{\mathrm{tr}(\boldsymbol{M})}{1-d}\right\rangle^2, \tag{9}$$

with M_i being the eigenvalues of $\boldsymbol{M}^{\mathrm{t}}$ and $\langle\bullet\rangle = \max\{\bullet, 0\}$ denoting the Macaulay brackets, is used to prevent damage evolution under compressive stress states. The damage part of the dissipation potential is specified as

$$\Phi^{\mathrm{d}}(\widehat{q}; d) = \frac{S}{s+1}\left\langle \frac{\widehat{q}-q_0}{S}\right\rangle^{s+1} \frac{1}{[\,1-d\,]^{\gamma}}\,, \tag{10}$$

where S, s, q_0 and γ are material parameters.

2.2 Gradient-enhanced Lemaitre-based model

For the gradient-enhanced damage approach a nonlocal damage variable ϕ is introduced as an additional field variable and linked to the local damage variable κ via a penalty term in the Helmholtz energy. Thereby, only the gradient of the nonlocal damage field ϕ needs to be taken into account, rather than the gradient of an internal variable stored at the integration point level within a finite element setting. The local damage variable κ shall be related to the local damage quantity d via

$$d(\kappa) = 1 - \exp(-\eta\,\kappa)\,, \tag{11}$$

with material parameter η. In contrast to d, which is limited to [0, 1), κ is positive but otherwise unbounded. Thus, additional constraints on the nonlocal damage field ϕ can be avoided. In the gradient-enhanced setting the Helmholtz energy has an additional nonlocal contribution, i.e. $\Psi = \Psi^{\mathrm{e}} + \Psi^{\mathrm{p}} + \Psi^{\mathrm{nloc}}$. The elastic energy is based on the logarithmic strains settled in the spatial configuration and, moreover, split into volumetric and isochoric contributions which are weighted by different damage contributions, namely

$$\begin{aligned}\Psi^{\mathrm{e}}(\boldsymbol{\varepsilon}^{\mathrm{e}}, d) = {}& [\,1-d\,]\,K\mathrm{tr}^2(\boldsymbol{\varepsilon}^{\mathrm{e}}) \\ & + [\,1-d^{\mathrm{iso}}\,]\,G\,\mathrm{tr}\Big(\boldsymbol{\varepsilon}^{\mathrm{e,iso}\,2}\Big)\,,\end{aligned} \tag{12}$$

with the definition $d^{\mathrm{iso}} := 1 - [\,1-d\,]^{n_{\mathrm{iso}}}$ where n_{iso} is an additional material parameter and K and G denote the compression and shear modulus. Proportional hardening is introduced similar to Swift-type hardening and determined by

$$\Psi^{\mathrm{p}}(\alpha) = \frac{h}{n_{\mathrm{p}}+1}\,\alpha^{n_{\mathrm{p}}+1}\,, \tag{13}$$

with hardening modulus h and hardening exponent $0 < n_{\mathrm{p}} \leq 1$. The nonlocal energy contributions are

$$\Psi^{\mathrm{nloc}} = \frac{c_{\mathrm{d}}}{2}\,\|\nabla_{\boldsymbol{x}}\phi\|^2 + \frac{\beta_{\mathrm{d}}}{2}\,[\,\phi-\kappa\,]^2\,, \tag{14}$$

with regularisation parameter c_{d} and penalty parameter β_{d}.

Instead of a single dissipation potential with a single Lagrange multiplier, as is used in the local model, the gradient-enhanced model is formulated as a multi-surface formulation, where plasticity and damage can evolve independently. The plastic dissipation potential is of von Mises type with an effective stress, i.e.

$$\Phi^{\mathrm{p}}(\boldsymbol{m}, \beta; d) = \frac{\|\mathrm{dev}(\boldsymbol{m}^{\mathrm{t}})\|}{[1-d]^{n_m}} - \sqrt{\frac{2}{3}}\,\big[\sigma_0^y - \beta\big]\,, \tag{15}$$

with material parameters n_m and σ_0^y. The damage dissipation potential is formulated in terms of the weighted damage driving force, namely

$$\widehat{q} := \langle \mathrm{tr}(\boldsymbol{\varepsilon}^{\mathrm{e}})\rangle^0\, q\,, \tag{16}$$

to incorporate the pressure insensitivity of damage evolution. The damage dissipation potential is then introduced as

$$\Phi^{\mathrm{d}}(q; d) = \widehat{q}\,\frac{\partial d}{\partial \kappa} - q_{\max}\,d^{n_{\mathrm{d}}}\,, \tag{17}$$

with damage threshold $q_{\max}$ and damage exponent n_{d}. For this multi-surface formulation two Lagrange multipliers λ^{p} and λ^{d} are introduced together with their respective KKT conditions connected to Φ^{p} and Φ^{d} respectively.

2.3 Finite element implementation

Both models are implemented into Abaqus using user subroutines. The local Lemaitre-type model is implemented via the subroutine 'VUMAT'. In the numerical implementation it is exploited that the subroutine interface provides the rate of deformation in the intermediate configuration $\boldsymbol{D}_0 = \boldsymbol{R}^{\mathrm{e}\,\mathrm{t}} \cdot \boldsymbol{d} \cdot \boldsymbol{R}^{\mathrm{e}}$ with $\boldsymbol{d} = \nabla_{\boldsymbol{x}}^{\mathrm{sym}} \dot{\boldsymbol{\varphi}}$. Here, $\boldsymbol{R}^{\mathrm{e}}$ represents the elastic rotation $\boldsymbol{R}^{\mathrm{e}} = \boldsymbol{F}^{\mathrm{e}} \cdot \boldsymbol{C}^{\mathrm{e}-1/2}$. Assuming small elastic strains, the elastic strain rate

$$\dot{\boldsymbol{E}}_0^{\mathrm{e}} = \boldsymbol{D}_0 - \boldsymbol{D}^{\mathrm{p}} \tag{18}$$

is approximated, see e.g. [5]. Updates of the stress tensor $\boldsymbol{M}$ and internal variables are then obtained by using a cutting plane algorithm. The algorithmic implementation follows [24]. The discretisation of the air bending process elaborated later on employs quadrilateral linear plane strain elements with reduced integration (Abaqus element type 'CPE4R').

In contrast to the explicit implementation of the local model (mass scaling factor 100), the gradient-enhanced model is implemented implicitly into the user subroutine 'UMAT'. In the algorithmic implementation the evolution equations need to be discretised in time. Time discretisation of the plastic velocity gradient $\boldsymbol{l}^{\mathrm{p}}$ is performed using an exponential map, while the evolution equations for α and d are discretised with an implicit backward-Euler scheme. The resulting two surface problem is solved by means of an active set algorithm.

Due to the presence of the additional nonlocal damage field ϕ in the gradient-enhanced model, an additional degree of freedom, beside the three displacement degrees of freedom, needs to be used. As discussed by Ostwald et al. [19], this is realised in Abaqus by using the temperature degree of freedom and additionally implementing the user subroutine 'UMATHT'. The discretisation is performed using a linear-linear brick element with eight integration points (Abaqus element type 'C3D8T').

3 Basic parameter identification

In order to match simulation results, respectively the models proposed, with experimental data a basic parameter identification shall be performed. In this context, the simulation and experimental investigation of a specimen under tensile loading is considered.

In particular, nine specimens with two circular notches, see Fig. 1, cut from a DP800 sheet with 1.5 mm thickness are subjected to tensile loading. From these nine specimens the experimental response of one specimen is chosen for parameter identification, since deviations between

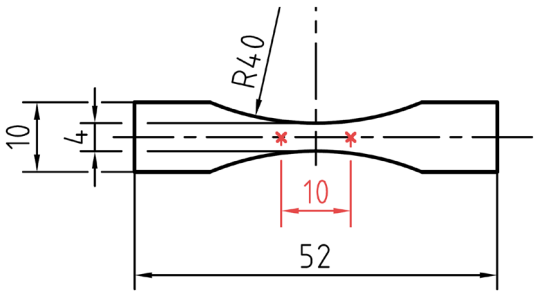

Fig. 1 Geometry of the tensile specimen used for parameter identification. The specimen is cut from a DP800 sheet with 1.5 mm thickness. Specifications in mm. The points chosen for elongation measurement via DIC are marked in red

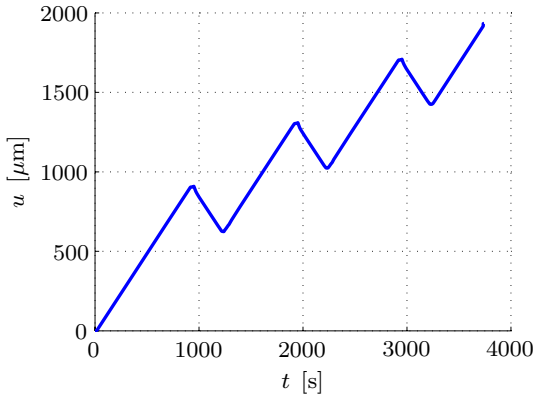

Fig. 2 Prescribed displacement loading of the tensile experiment. Displacement u in µm over time in s

data obtained from different specimens are small (less than 0.5%). The loading is applied by prescribing a linearly increasing displacement of the clamping with the loading path being three times interrupted in order to include elastic unloading, see Fig. 2. The force is measured by a 10 kN load cell and displacements are measured by means of a virtual extensometer. The specimen is recorded by a camera and via digital image correlation (DIC) the elongation between two virtually chosen points is determined. In this case, two points within the centerline, respectively tensile axis and with an initial distance of 10 mm are chosen.

The finite element discretisation includes one eighth of the specimen by making use of symmetry properties. For the simulations, only monotonic loading is considered. It is applied by prescribing the optically measured displacements (at the points marked in red in Fig. 1) excluding the elastic unloading. The total longitudinal force response of the simulation, F_t^{sim}, is compared to the force measured in the experiment, F_t^{exp}, at each point in time t. The comparison of both motivates the objective function

$$o(\boldsymbol{k}) = \sum_{t=0}^{n} \left[F_t^{\mathrm{sim}}(\boldsymbol{k}) - F_t^{\mathrm{exp}} \right]^2 , \tag{19}$$

with $\boldsymbol{k}$ representing the respective set of material parameters. In view of the parameter identification process, a generalised simplex algorithm minimises the objective function $o(\boldsymbol{k})$ by varying the material parameters.

Common values for the elastic parameters E and ν of steel are chosen. The parameter identification of the local Lemaitre-type model is set up to determine all seven inelastic parameters, see Table 1, and is based on a discretisation with a characteristic element edge length $l_\mathrm{e} = 0.05$ mm. The gradient-enhanced model includes ten inelastic parameters of which, however, only six parameters are determined by the parameter identification procedure, since only integral information, i.e. the reaction forces, are included in the objective function. Additional parameters can be identified if the displacement field is part of the objective function as well. All plastic parameters—σ_0^y, h and n_p—are part of the identification process. In view of the damage related parameters though, only q_max, η and n_m are to be determined by the parameter identification. The damage exponent n_d is fixed at 0.6667 as it has very little influence on the response. The parameter n_iso is empirically chosen as $n_\mathrm{iso} = 0.5$. The regularisation parameter c_d is fixed at 0.5 guaranteeing a sufficient regularisation while the penalty parameter β_d is fixed at 100.0, chosen such that local and non-local damage fields match. The values of all parameters are listed in Table 2.

The related load-displacement responses of the simulations with the identified parameters are plotted against experimental data in Fig. 3, revealing good agreement between experiment and simulations. The underlying simulations are performed with a discretisation of 24,300 elements of characteristic element (edge) length $l_\mathrm{e} = 0.05$ mm. Related contour plots of the damage variable d of the local model, cf. Eqs. (4, 9, 10), and the damage variable $d^\mathrm{iso} := 1 - [\,1 - d\,]^{n_\mathrm{iso}}$ of the gradient-enhanced model, cf. Eqs. (4, 16, 17), are shown in Fig. 4 for different discretisations—to be specific, the fine mesh with $l_\mathrm{e} = 0.05$ mm and 24,300 elements used for the parameter identification, a discretisation with $l_\mathrm{e} = 0.1$ mm and 4752 elements, and a coarse mesh with $l_\mathrm{e} = 0.2$ mm and 880 elements.

Table 1 List of all material parameters for the local Lemaitre-type model

Symbol	Name	Value	Unit
E	Young's modulus	208.00	GPa
ν	Poisson's ratio	0.30	–
α_0	initial hardening	0.000287	–
A	hardening modulus	1333.0	MPa
n	hardening exponent	0.1537	–
q_0	damage threshold	0.09738	MPa
s	damage exponent	2.16	–
S	damage factor	4.37	MPa
γ	pre-damage influence	6.98×10^{-5}	–

Table 2 List of all material parameters for the gradient-enhanced Lemaitre-type model

Symbol	Name	Value	Unit
E	Young's modulus	208.00	GPa
ν	Poisson's ratio	0.30	–
σ_0^y	initial yield stress	165.66	MPa
h	hardening modulus	1611.24	MPa
n_p	hardening exponent	0.2436	–
q_max	damage threshold	1.5162	MPa
n_d	damage exponent	0.6667	–
η	damage factor	0.5092	–
n_iso	isochoric damage factor	0.5	–
n_m	effective stress factor	0.3128	–
c_d	regularisation parameter	0.5	–
β_d	penalty parameter	100.0	–

In contrast to the quasi-identical load-displacement response shown in Fig. 3, the damage distributions resulting from the local and the gradient-enhanced damage model significantly differ, see Fig. 4a, d. Moreover, the local model shows strongly mesh dependent behaviour, whereas the gradient-enhanced model results in mesh independent results in view of the different discretisations considered, see Fig. 4. To be specific, in the case of the local model, localisation of the damage distribution occurs in a region related to the, say, first element row in the cross-sectional symmetry plane

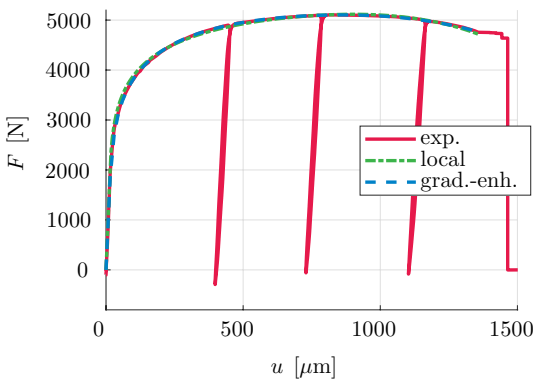

Fig. 3 Load–displacement curves comparing the responses of the simulation after parameter identification with the tensile experiment. Reaction force F in N over displacement u in µm. The red curve represents experimental data, the green curve shows the response of the simulation with the local Lemaitre model and the blue curve shows the response of the gradient-enhanced damage model (color figure online)

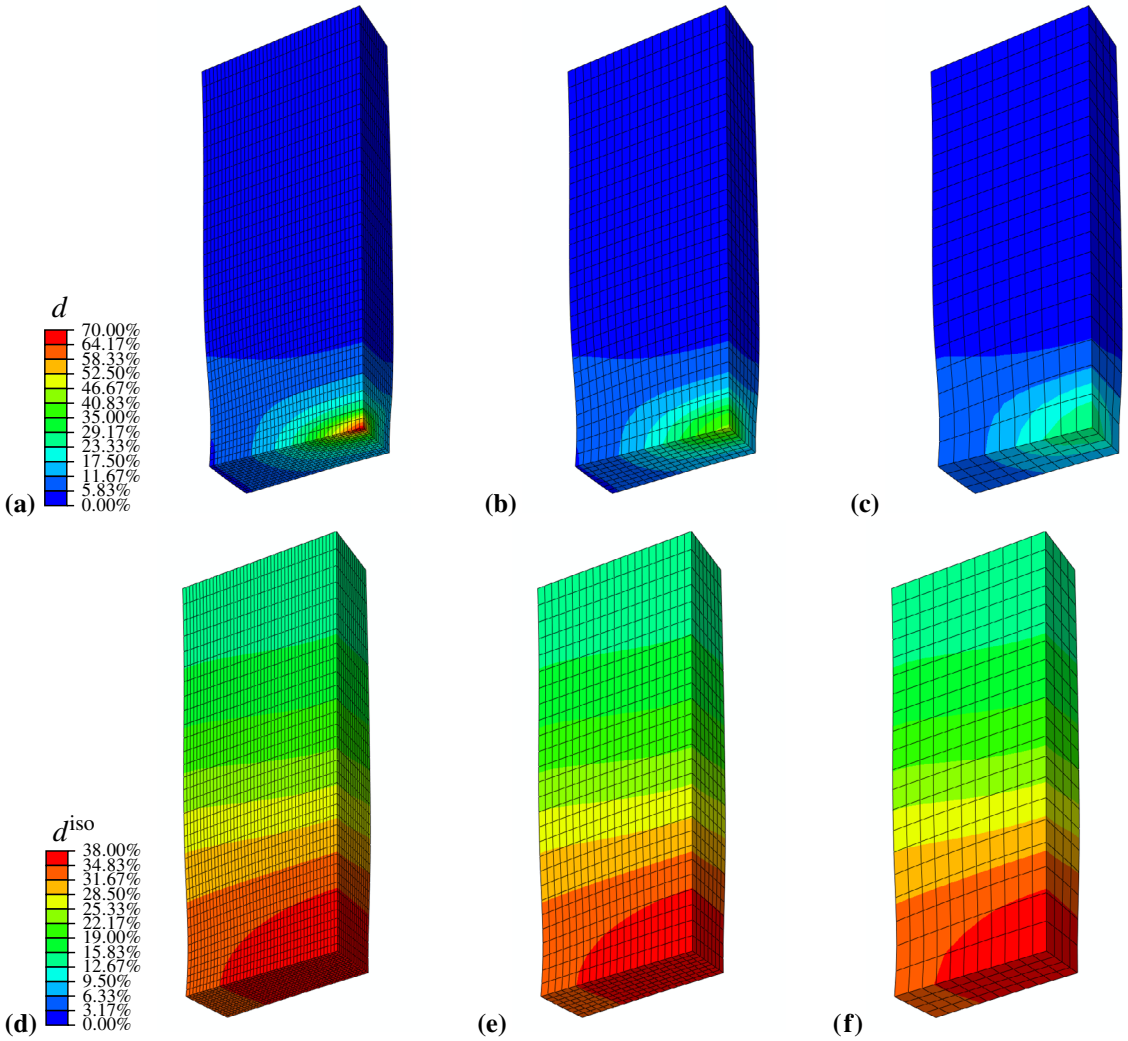

Fig. 4 Contour plots for deformed meshes (one eighth of the specimen) at the last load step of the applied tensile loading: Distribution of damage variable d for the local model **a**–**c** and damage variable d^{iso} for the gradient-enhanced model **d**–**f** for three different discretisations, i.e. $l_e = 0.05$ mm: **a** and **d**, $l_e = 0.1$ mm: **b** and **e**, $l_e = 0.2$ mm : **c** and **f**

of the specimen, while the gradient-enhanced model shows quasi-identical damage distributions for the three different meshes chosen. In addition, the maximum damage value vastly increases for the local model with a finer discretisation, whereas the gradient-enhanced models renders the maximum damage value quasi-independent of the discretisation. This underlines the high mesh dependency of the local Lemaitre-type damage model. Furthermore, the parameter identification in general provides different parameter values for different meshes in the case of the local model, which is most relevant for applications and process simulations.

4 Air bending

Both, the local and the gradient-enhanced damage model shall next be demonstrated by means of a simulation of an air bending process. To this end, an air bending experiment as illustrated in Fig. 5 is considered. To be specific, an unlubricated DP800 steel sheet ($50 \times 100 \times 1.5$ mm) is bent such that the bending line is parallel to the rolling direction. The experiment is performed with a Zwick Z100 universal testing machine and with a punch radius

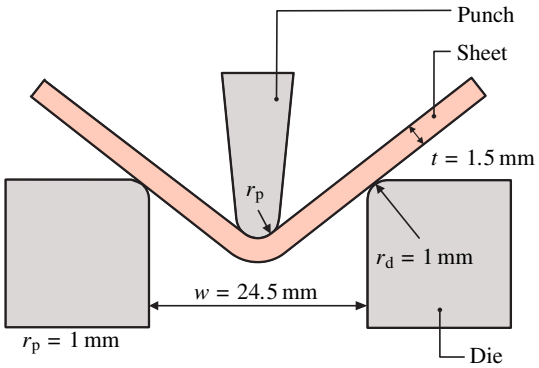

Fig. 5 Experimental set up of the air bending process of a DP800 sheet

of $r_p = 1$ mm. Moreover, the punch displacement is measured by a tactile transducer. The die width considered is $w = 24.5$ mm and the die radius is $r_d = 1$ mm.

The set up for the simulation assumes plane strain conditions and uses symmetry. Punch and die are discretised with rigid elements, whereas the sheet itself is discretised with linear quadrilateral plane strain elements. Contact is defined between die and sheet as well as between punch and sheet. The contact formulation for the explicit local model is enforced with a penalty method, while for the implicit gradient-enhanced model a Lagrange multiplier formulation is used. The die is fixed in space and the punch displacements are prescribed. The sheet has prescribed symmetry boundary conditions and is otherwise held in place by contact with the die and loaded by contact with the punch. In order to study mesh independence, the bending region of the sheet is discretised with two different meshes: a reference mesh with an element edge length of $l_e = 0.05$ mm and a fine mesh with $l_e = 0.025$ mm.

Figure 6 illustrates the damage evolution during loading in the outer fibres of the bent sheet for both models and the two different discretisations considered. The results show that no significant mesh dependencies can be observed for the damage evolution at the particular material point considered. The maximum damage values obtained from the two different models differ, Fig. 6. At this stage, however, neither a comparison of the modelling details of both models nor a comprehensive comparison of each model to the experimental response is the focus or in the scope of this contribution. Hence, the load displacement curves of the local model (explicit formulation) and the gradient-enhanced model (implicit formulation), see Fig. 7, are shown here for the sake of completeness. A qualitative agreement between each simulation and the experimental response can be observed—quantitatively, differences remain. These can (probably) be explained by the basic parameter identification based on a tensile experiment, which does not enable a suitable identification of all material parameters, since strain amplitude and stress mode in the air bending process are vastly different compared to the tensile experiment used for the parameter identification. The kinks, or rather the zig-zag-pattern, in the load displacement curves generated with the local model can be attributed to the discretisation of the contact between sheet and die and are amplified by mass scaling in the explicit simulations. By analogy with Fig. 6, the load displacement diagram shows no significant mesh dependencies. Similarly, the contour plots of the damage variable d of the local model shown in Fig. 8a, c do not

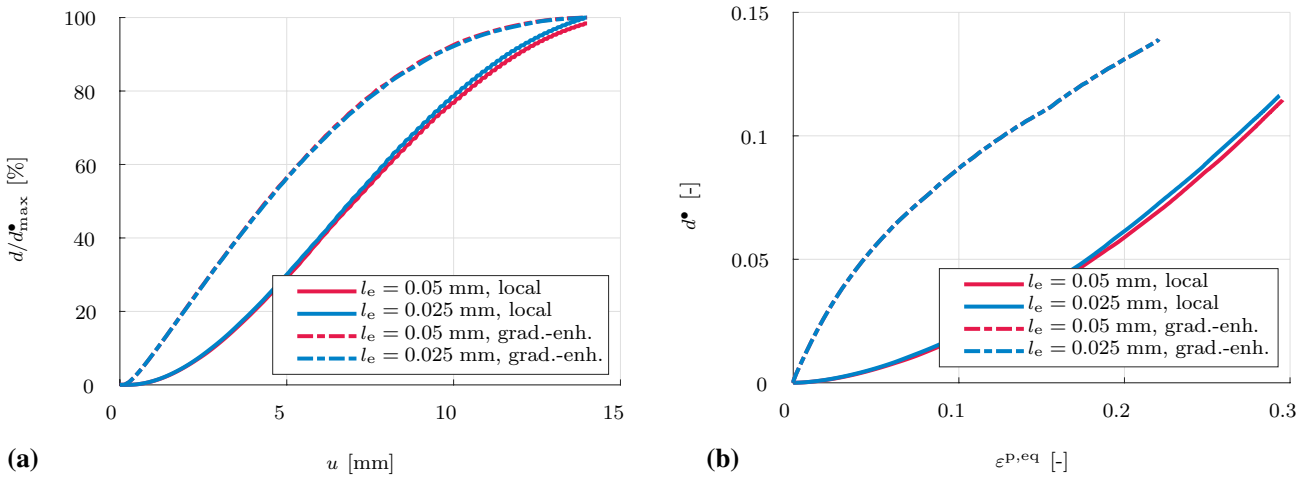

Fig. 6 Comparison of damage evolution at the lower left corner node (outmost layer in the symmetry plane, cf. Figs. 8 and 9) for both models and two different discretisations. In the left diagram (**a**), normalised damage is plotted over punch displacement. For the local model, damage variable d is normalised with respect to the maximum value in the finer mesh, $d^{\mathrm{loc}}_{\mathrm{max}} = 11.63\%$. For the gradient-enhanced model, damage variable d^{iso} is normalised with respect to the maximum value in the finer mesh, $d^{\mathrm{grad}}_{\mathrm{max}} = 14.06\%$. The right diagram, **b**, shows damage variable d for the local model and d^{iso} for the gradient enhanced-model plotted over equivalent plastic strain

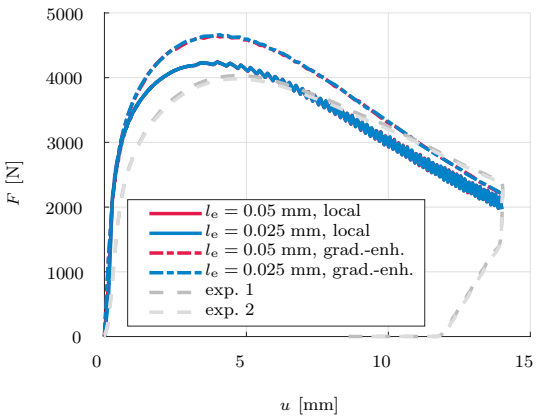

Fig. 7 Load displacement curves of the air bending experiment and the corresponding simulation results of the implicit gradient-enhanced model and the explicit local model for two different discretisations. Oscillations occur because of mass scaling in the explicit simulations. These can be reduced by lowering mass scaling at the cost of significantly increasing computation time

indicate significant mesh dependencies due to the particular bending mode investigated here. As expected, the damage distribution of d^{iso} generated by the gradient-enhanced model turns out to be mesh independent, see Fig. 8b, d. In the contour plots of the proportional hardening variable α, see Fig. 9, a similar behaviour becomes apparent.

The quasi mesh independent behaviour of the local model shown in Fig. 8 is in contrast to the response of the local model discussed above in the context of the boundary-value problem investigated within the parameter identification, see Sect. 3. In other words, the particular bending deformation analysed and geometry chosen here generates almost no necking or rather localisation modes such as the tension-dominated loading setup elaborated for the parameter identification. Moreover, the bending problem is simulated under plane strain conditions, which additionally further suppresses related localisation modes for the particular boundary-value problem considered here.

In general, however, air bending may lead to considerable localisation. Heibel et al. [11] investigated different high-strength steels with the VDA bending test, [29]. Localisation was observed for complex phase steels, which exhibit a less pronounced hardening compared to the DP800 steel analysed in the current paper. It is remarked that process parameters such as the width between the rollers, punch displacement and corresponding bending angle are different in the VDA test and may lead to differences in localisation behaviour. For bending problems showing localisation, mesh size dependent damage evolution was observed by Soyarslan et al. [24].

In order to increase localisation for the air bending setup discussed in Fig. 5, the width of the die in the simulations

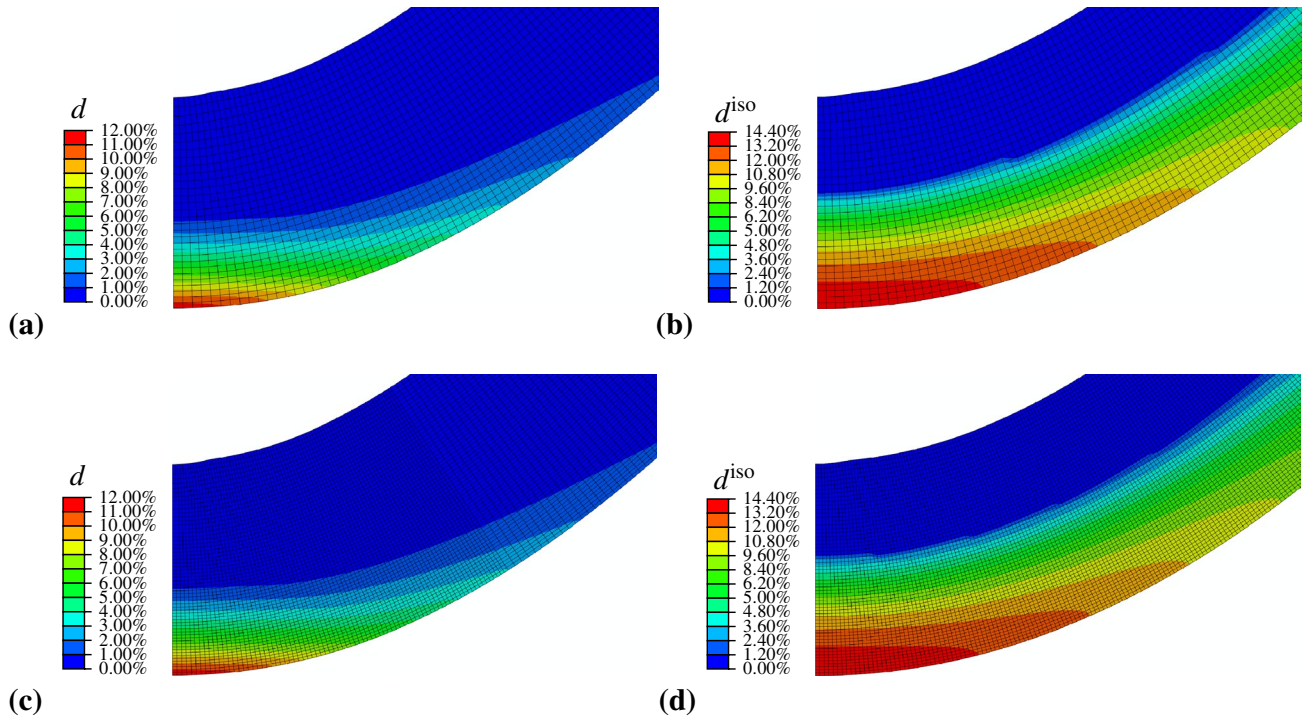

Fig. 8 Contour plots for deformed meshes at punch displacement 14 mm of the air bending simulation with die width $w = 24.5$ mm: distribution of damage variable d for the local model (**a**, **c**) and damage variable d^{iso} for the gradient-enhanced model (**b**, **d**) for two different discretisations—$l_e = 0.05$ mm: **a** and **b** $l_e = 0.025$ mm: **c** and **d**

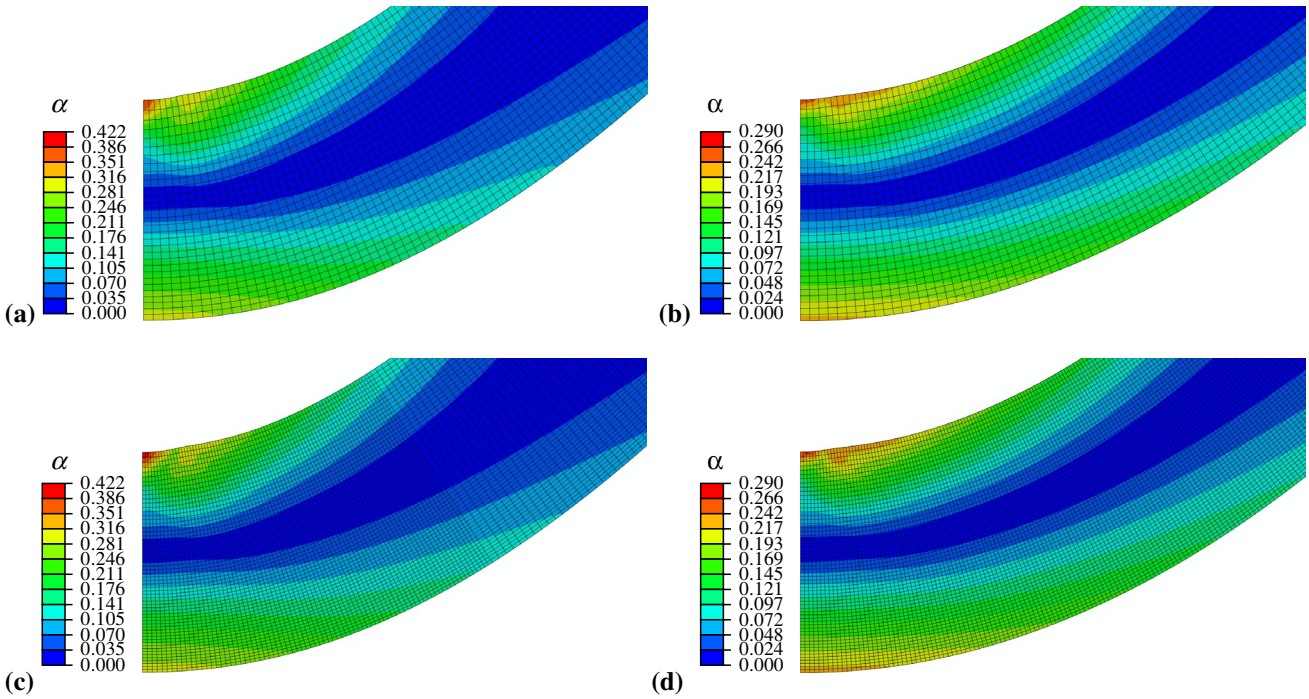

Fig. 9 Contour plots for deformed meshes at punch displacement 14 mm of the air bending simulation with die width $w = 24.5$ mm: distribution of the proportional hardening variable α for the local model (**a**, **c**) and the gradient-enhanced model (**b**, **d**) for two different discretisations – $l_e = 0.05$ mm: **a** and **b**, $l_e = 0.025$ mm: **c** and **d**

is reduced to $w = 16$ mm. The responses of two different discretisations with element edge lengths of $l_e = 0.05$ mm and $l_e = 0.025$ mm are compared. The simulation results are depicted in Figs. 10 and 11 by means of the distribution of damage and the distribution of the proportional hardening variable. One immediately notices a significant mesh dependence of both damage distribution and distribution of the hardening variable for the local model. This can be attributed to the stronger localisation resulting in much higher maximum values of damage and proportional hardening variable for the local model compared to the previous setup with a die width of $w = 24.5$ mm. The stronger localisation in the local model is emphasized by a difference in the deformation behaviour. The bending radius is smaller for the local model compared to the mesh independent response of the gradient-enhanced model.

5 Summary

In the context of finite element simulations, local continuum damage formulations lead to mesh dependent results. Typically, metal forming simulations are performed using a fixed (sometimes quite small) element size for which material parameters are fitted based on experimental data. In general, the values of the material parameters of a local damage model depend on the particular discretisation and mesh size chosen. A different, mathematically more refined and rigorous approach employs regularised continuum damage models which, however, may require higher computational effort. Since such gradient-enhanced models result in mesh independent simulation results, material parameters only need to be identified once for the particular material considered and the mesh size can be varied more flexibly. Thereby, the overall computational effort can be reduced.

In the present contribution the continuum damage framework for Lemaitre-type damage modelling is briefly introduced and the underlying energies and potentials for a local as well as a regularised gradient-enhanced model are specified. Both models are implemented into the commercial finite element software Abaqus by means of user subroutines for user defined material behaviour. A suitable parameter set to predict the behaviour of DP800 steel sheets is determined via a basic parameter identification using experimental data of a tensile test. For this tensile loading state, which results in inhomogeneous states of deformation, significant mesh dependencies for both distribution and maximum value of the damage variable were shown in the responses of the simulations with the local model. This also means the identified parameters for the local model are dependent on the chosen discretisation. For both models two air bending processes with different die widths were simulated under plane strain conditions. The load displacement response, damage evolution over time as well as the contour plots of the distribution

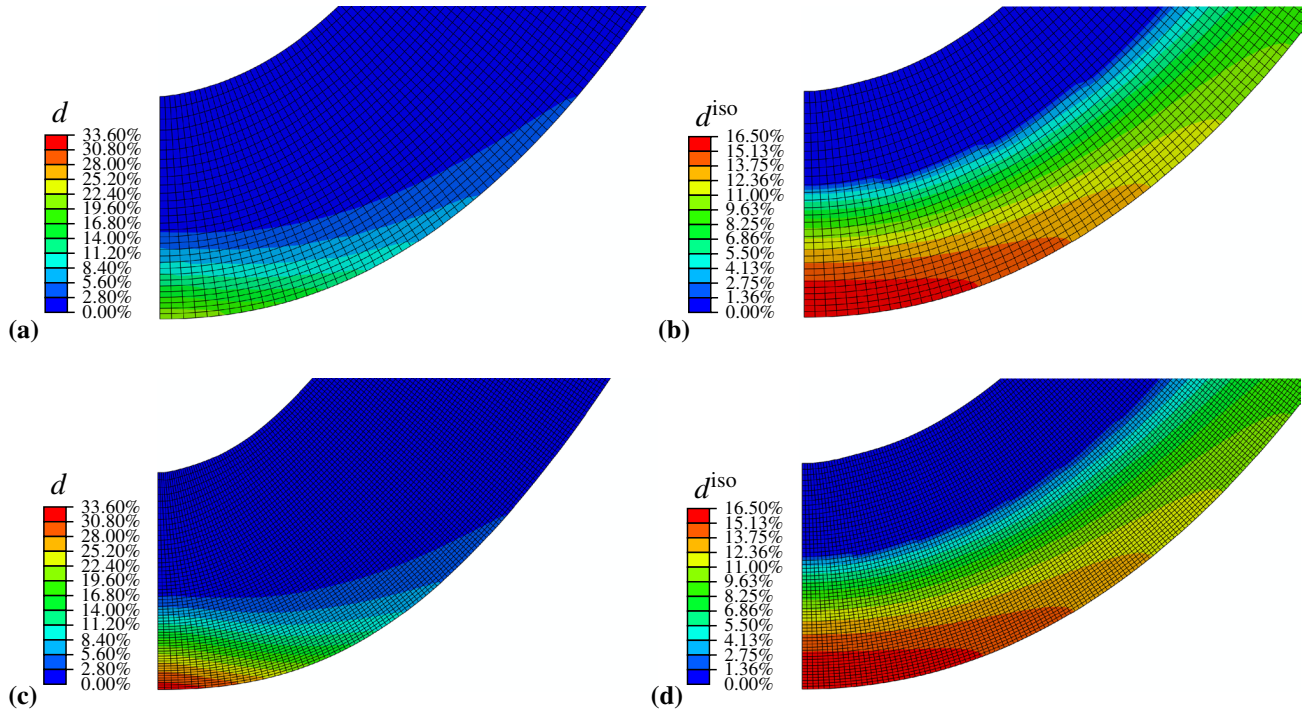

Fig. 10 Contour plots for deformed meshes at punch displacement 14 mm of the air bending simulation with die width $w = 16$ mm: distribution of damage variable d for the local model (**a**, **c**) and the gradient-enhanced model (**b**, **d**) for two different discretisations – $l_e = 0.05$ mm: **a** and **b**, $l_e = 0.025$ mm: **c** and **d**

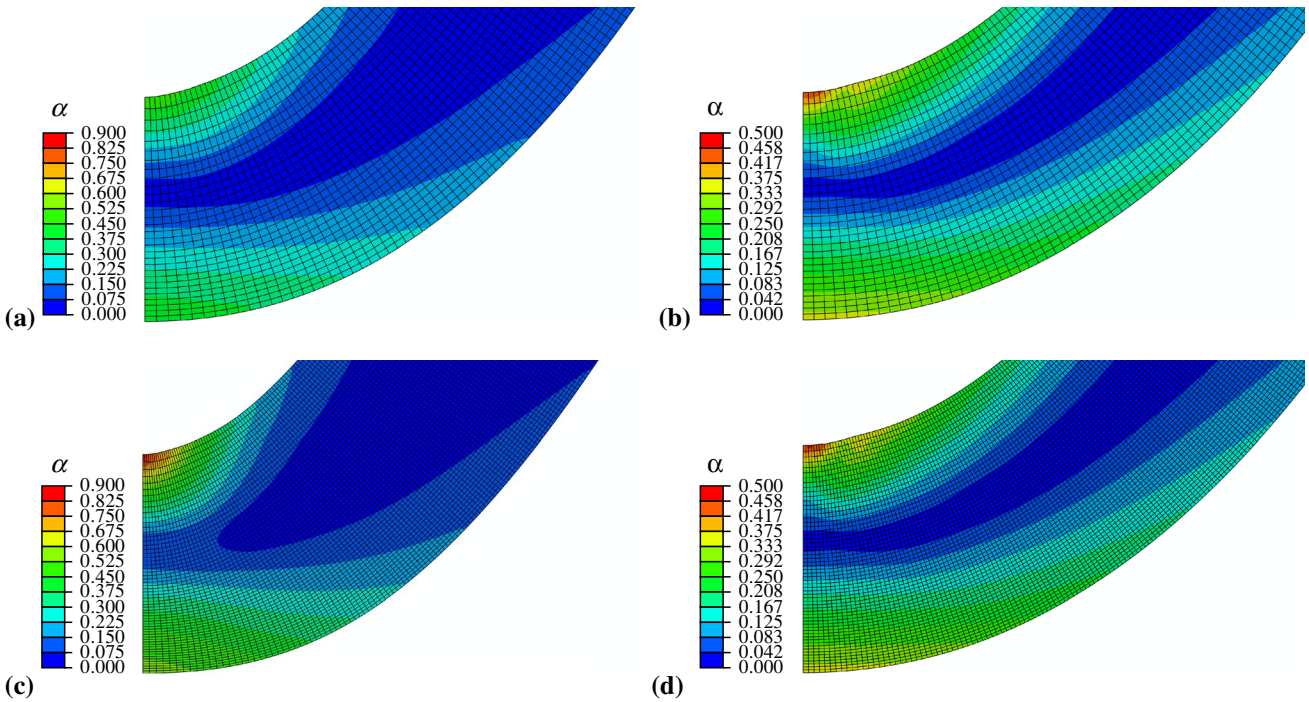

Fig. 11 Contour plots for deformed meshes at punch displacement 14 mm of the air bending simulation with die width $w = 16$ mm: distribution of the proportional hardening variable α for the local model (**a**, **c**) and the gradient-enhanced model (**b**, **d**) for two different discretisations—$l_e = 0.05$ mm: **a** and **b**, $l_e = 0.025$ mm: **c** and **d**

of the simulated damage variable and the proportional hardening variable confirm the mesh independence of the gradient-enhanced model. While the simulation with the local model of the air bending process with the larger die width appears to be less sensitive to the different discretisations, respectively element sizes, the altered air bending process with smaller die width revealed a significant mesh dependency of the local model. It appears, the mesh dependency of the local model is strongly dependent on the specific loading and deformation modes activated, thus making it difficult to a priori determine the validity of a simulation response of the local model.

Future research work shall focus on matching simulation response and experiment by extending the constitutive model on the one hand and on the other hand improving the parameter identification process. The very basic pressure insensitivity of damage evolution introduced in the gradient-enhanced model can be replaced by micro-mechanically motivated approaches. For load cases with multi-axial loading the incorporation of kinematic hardening effects have to be considered. The parameter identification shall be improved by incorporating the displacement field obtained via DIC into the objective function. Moreover, additional experiments can be taken into account, e.g. compression tests or experiments combining tension and torsion loading in order to activate different loading and deformation modes as well as interactions of these modes.

Acknowledgements Funded by the Deutsche Forschungsgemeinschaft (DFG, German Research Foundation)—Projektnummer 278868966—TRR 188—Projects A05, C02 and S01.

References

1. Akeret R (1978) Versagensmechanismen beim Biegen von Aluminiumblechen und Grenzen der Biegefähigkeit. Aluminium 54:117–123
2. Bažant ZP, Belytschko TB, Chang T-P (1984) Continuum theory for strain-softening. J Eng Mech 110(12):1666–1692
3. Bažant ZP, Pijaudier-Cabot G (1988) Nonlocal continuum damage, localization instability and convergence. J Appl Mech 55(2):287–293
4. Cao TS (2017) Models for ductile damage and fracture prediction in cold bulk metal forming processes: a review. Int J Mater Form 10(2):139–171
5. Clausmeyer T, Güner A, Tekkaya AE, Levkovitch V, Svendsen B (2015) Modeling and finite element simulation of loading-path-dependent hardening in sheet metals during forming. Int J Plast 63:64–93
6. De Borst R, Sluys LJ, Mühlhaus H-B, Pamin J (1993) Fundamental issues in finite element analyses of localization of deformation. Eng Comput 10(2):99–121
7. Dimitrijevic BJ, Hackl K (2008) A method for gradient enhancement of continuum damage models. Technische Mechanik 28(1):43–52
8. El Budamusi M, Becker C, Clausmeyer T, Gebhard J, Chen L, Tekkaya AE (2015) Erweiterung der Formänderungsgrenzen von höherfesten Stahlwerkstoffen bei Biegeumformprozessen durch innovative Prozessführung und Werkzeuge. Bericht zum Vorhaben IGF-Nr. 16585 N/FOSTA P930, https://shop.stahldaten.de/produkt/p-930-erweiterung-der-formaenderungsgrenzen-von-hoeherfesten-stahlwerkstoffen-beibiegeumformprozessen-durch-innovative-prozessfuehrung-und-werkzeuge
9. Forest S (2009) Micromorphic approach for gradient elasticity, viscoplasticity, and damage. J Eng Mech 135(3):117–131
10. Gurson AL (1977) Continuum theory of ductile rupture by void nucleation and growth: part I—yield criteria and flow rules for porous ductile media. J Eng Mater Technol 99(1):2–15
11. Heibel S, Dettinger T, Nester W, Clausmeyer T, Tekkaya AE (2018) Damage mechanisms and mechanical properties of high-strength multiphase steels. Materials 11(5):761
12. Kaupper M, Merklein M (2013) Bendability of advanced high strength steels—a new evaluation procedure. CIRP Ann 62(1):247–250
13. Kiefer B, Waffenschmidt T, Sprave L, Menzel A (2018) A gradient-enhanced damage model coupled to plasticity—multi-surface formulation and algorithmic concepts. Int J Damage Mech 27(2):253–295
14. Krajcinovic D (1996) Continuum models. In: Krajcinovic D (ed) Damage mechanics, vol 41. North-Holland series in applied mathematics and mechanics. North-Holland, Amsterdam, pp 415–602 (chapter 4)
15. Larsson R, Razanica S, Josefson BL (2016) Mesh objective continuum damage models for ductile fracture. Int J Numer Methods Eng 106(10):840–860
16. Lemaitre J (1985) A continuous damage mechanics model for ductile fracture. J Eng Mater Technol 107:83–89
17. Lemaitre J (1996) A course on damage mechanics. Springer, Berlin
18. Meya R, Löbbe C, Tekkaya AE (2019) Stress state analysis of radial stress superposed bending. Int J Precis Eng Manuf 20(1):53–66
19. Ostwald R, Kuhl E, Menzel A (2019) On the implementation of finite deformation gradient-enhanced damage models. Comput Mech 64(Issue 3):847–877
20. Peerlings R H J, de Borst R, Brekelmans W A M, de Vree J H P, Spee I (1996) Some observations on localisation in non-local and gradient damage models. Eur J Mech A Solids 15:937–953
21. Polindara C, Waffenschmidt T, Menzel A (2017) A computational framework for modelling damage-induced softening in fibre-reinforced materials—application to balloon angioplasty. Int J Solids Struct 118–119:235–256
22. Rousselier G (1987) Ductile fracture models and their potential in local approach of fracture. Nucl Eng Des 105(1):97–111
23. Sarkar J, Kutty TRG, Conlon KT, Wilkinson DS, Embury JD, Lloyd DJ (2001) Tensile and bending properties of AA5754 aluminum alloys. Mater Sci Eng A 316(1–2):52–59
24. Soyarslan C, Malekipour Gharbi M, Tekkaya A E (2012) A combined experimental–numerical investigation of ductile fracture in bending of a class of ferritic-martensitic steel. Int J Solids Struct 49(13):1608–1626
25. Soyarslan C, Tekkaya AE, Akyuz U (2008) Application of continuum damage mechanics in discontinuous crack formation: forward extrusion chevron predictions. ZAMM Zeitschrift für Angewandte Mathematik und Mechanik 88(6):436–453
26. Sprave L, Menzel A (2018) Gradient-enhanced ductile damage—a finite deformation framework with application to DP800. PAMM 18(1):e201800232
27. Triantafyllidis N, Aifantis E C (1986) A gradient approach to localization of deformation. I. hyperelastic materials. J Elast 16(3):225–237
28. Tvergaard V, Needleman A (1984) Analysis of the cup-cone fracture in a round tensile bar. Acta Metall 32(1):157–169

29. VDA 238-100 Plate bending test for metallic materials (2017). In: Verband der Automobilindustrie eV (ed). Berlin, Germany. https://www.vda.de/en/services/Publications/vda-238-100-plate-bending-test-for-metallic-materials.html
30. Wcislo B, Pamin J, Kowalczyk-Gajewska K (2013) Gradient-enhanced damage model for large deformations of elastic–plastic materials. Arch Mech 65(5):407–428